Numerical Analysis of Combustion Field in Hybrid Rocket Motor with Swirling and Axial Oxidizer Injection

Mikiro Motoe⋆, *Tomoki Matsuno*⋆ *and Toru Shimada*⋆†
⋆*Japan Aerospace Exploration Agency*
3-1-1 Yoshinodai, Chuo, Sagamihara, Kanagawa 252-5210, Japan
motoe.mikiroh@jaxa.jp · matsuno.tomoki@ac.jaxa.jp · shimada.toru@jaxa.jp
†Corresponding author

Abstract

Large Eddy Simulations have been conducted on combustion flows inside a hybrid rocket with swirling and tangential oxidizer injections from upstream end. The bulk, axial and radial characteristics of the flow field are investigated and confirmed the mixing promotion and the fuel regression rate improvement due to the swirling flow. Central axial jet injection has a suppression effect by inducing a unique flow field. By changing the injection mass-flow ratio of the axial and tangential, even at the same total flow rate, the flow characteristics change the thrust and O/F as the effective swirl number changes.

1. Introduction

One of the technological innovations for future space transport is the safety of space transportation, for which hybrid rocket propulsion will play an important role as an essentially non-explosive propulsion system. So many research and development have been and are currently under way in order to overcome technical challenges of current hybrid rockets; fuel regression rate, combustion efficiency, combustion stability, O/F-shift, etc. [1]. In particular, the problem of O/F shift is not only a drawback in propulsion performance but also a non-negligible issue that leads to propellant residue [2]. In recent research, as a promising measure capable of solving these issues at once, expected is a technique for simultaneously controlling both the thrust and the O/F by independently manipulating axial and tangential oxidizer injection mass flow rates; for example, as in Altering-intensity Swirling-Oxidizer-Flow-Type (A-SOFT) hybrid rockets [3]. A schematic of A-SOFT is shown in Fig.1.
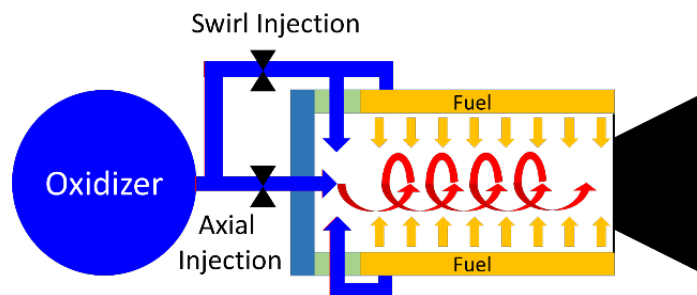
Figure 1: Schematic of A-SOFT hybrid rocket

The combustion of hybrid rockets is characterized by a diffusion flame in the turbulent boundary layer formed by the oxidizer flow over the fuel surface. Furthermore, in this paper more specifically, we will consider swirling turbulent oxidizer flows. Generally, in turbulent flow, turbulent transport is accompanied by anisotropy according to the geometric characteristics of mean flow. This also holds true in swirling turbulent flows, that is the turbulent diffusion in the radial direction is significantly suppressed[4].

Numerical simulations on the combustion flow of Swirling-Oxidizer-Flow-Type (SOFT) hybrid rockets have been carried out by Motoe and Shimada [5]. In the present study, with slight modifications made to the previous computational method, we have conducted three new simulations for A-SOFT hybrid rockets with different flow-rate

ratios of the axial and the tangential oxidizer injections. We will describe the findings obtained from these computation in this paper.

2. Outline of flow simulation

2.1 Assumptions and methods of simulation

There are several methods of dealing with turbulence. Among them, Large-Eddy Simulation (LES) is chosen here. That is, temporal evolution of a large scale fluid structure above the spatial grid resolution is directly obtained from the spatially filtered Navier-Stokes equation and fluid behavior below the spatial grid resolution is modeled.

    The flow Mach number in the combustion chamber is low, whereas the combustion chamber temperature is sufficiently high, so the relaxation time due to the chemical reaction is extremely short compared to that due to flow dynamics. In such a case, the flow evolution simulation and the chemical reaction calculation can be separated, and the approximation that the chemical reaction reaches the steady state corresponding to the local environment at each moment in time evolution of the flow simulation is appropriate. Based on such a premise, it becomes possible to separate the simulation into two; one is advection and diffusion simulation of mixture fraction based on the presence of carbon, which is a component of fuel, and the other is local laminar counterflow diffusion flame calculation. This method is known as the Flamelet method [6, 7, 8]. In making a flamelet table, we have employed a detailed chemical reaction model of GRI-MECH 3.0 [9] where 53 chemical species and 325 elementary reactions are considered. In the fluid simulation, we assume the gas mixture is composed of 31 chemical species with 22 chemical species negated because the amount was small over all the tables.

2.2 Governing equations and numerical methods

The governing equations of LES are transport equations of filtered compressible Navier-Stokes equations (conservations of mass, momentum, and energy) and fuel mixture fraction as shown in Eqs.(1, 2, 3, and 4).

$$\frac{\partial \bar{\rho}}{\partial t} + \frac{\partial \bar{\rho}\tilde{u}_j}{\partial x_j} = 0, \tag{1}$$

$$\frac{\partial \bar{\rho}\tilde{u}_i}{\partial t} + \frac{\partial \bar{\rho}\tilde{u}_i\tilde{u}_j}{\partial x_j} = -\frac{\partial \hat{p}}{\partial x_i} + \frac{\partial}{\partial x_j}\,\tilde{\tau}_{ij} + \tau_{sgs_{ij}}\,, \tag{2}$$

$$\frac{\partial \bar{\rho}\tilde{e}}{\partial t} + \frac{\partial \bar{\rho}\tilde{u}_j\tilde{H}}{\partial x_j} = \frac{\partial}{\partial x_j}\,\tilde{u}_i\tilde{\tau}_{ij} - \tilde{q}_j - q_{sgs_j}\,, \tag{3}$$

$$\frac{\partial \bar{\rho}\tilde{\xi}}{\partial t} + \frac{\partial \bar{\rho}\tilde{u}_j\tilde{\xi}}{\partial x_j} = \frac{\partial}{\partial x_j}\left(\bar{\rho}D_c\frac{\partial \tilde{\xi}}{\partial x_j}\right), \tag{4}$$

where t is the time, $x_i(i = 1, 2, 3)$, the spatial coordinates, ρ, the density, $u_i(i = 1, 2, 3)$, the velocity components, p, the pressure, τ_{ij}, the stress tensor elements, e, the specific total energy, H, the total enthalpy, $q_i(i = 1, 2, 3)$, the heat flux components, ξ, the mixture fraction, and D_c, the diffusion coefficient. Spatially filtered quantities are represented by ($\hat{\cdot}$) and density-weighted (Favre) filtered quantities are represented by ($\tilde{\cdot}$). The subscript sgs represents sub-grid-scale terms.

    In numerical analysis, the governing equations (1) - (4) are spatially discretized by the finite volume method, and the simultaneous ordinary differential equations obtained for each finite volume (cell) are time-integrated to evaluate the instantaneous cell-averaged values of the density, the momentum, the total energy, and the fuel mixture fraction. For the numerical flux of the convection term, SLAU method [10] is adopted to suppress the numerical diffusion in the low Mach number flow. In order to efficiently reduce the calculation cost, in the early stage of the calculation, a third-order-accurate MUSCL reconstruction at the cell boundary. Once the flow field inside the chamber develops well, then, in order to increase the spatial resolution, the fifth-order-accurate WENO-Z scheme [11] takes turns. For the time integration, ADI-SGS scheme [12] with the dual time step method [13] using the second-order backward difference method is adopted. For the subgrid-scale turbulence modeling WALE model [14] is used.

    In one time step, based on the instantaneous flow field updated by the time-integration, combustion calculation is made by looking-up the Flamelet table using the fuel mixture fraction ξ and its dissipation rate χ evaluated by

$$\chi = 2D_c\,\left(\frac{\partial \xi}{\partial x}\right)^2 + \left(\frac{\partial \xi}{\partial y}\right)^2 + \left(\frac{\partial \xi}{\partial z}\right)^2\,. \tag{5}$$

From the Flamelet table, the mass fraction of each chemical species, the transport coefficients for the gas mixture are obtained. Then, the temperature and the pressure are calculated from the energy and the chemical species densities, thus feeding back the effect of combustion to the flow field. By repeating the above steps on a time-evolutionary basis, the combustion flow field is calculated.

3. A-SOFT hybrid rocket engine simulations

3.1 Computational domain

For the computational domain shown in Fig. 2, simulation is performed so as to follow the time evolution of the flow field at each moment. Geometric parameters are summarized in Table 1. The total length of the combustion chamber is 175 mm, the tangential injectors are located at the position of eight equally divided in the circumferential direction and at 1 mm away from the upstream end in the axial direction. There are 8 oxidizer inlets each of the size of $3mm \times 2.55mm$ for the tangential injections, where 2.55 mm is the height of the duct cross section and the opening angle in the circumferential direction is 29.25 degrees. So in total by 8 outlets, 65% of the whole circumference has openings. The outlet is like a scarf nozzle and is cut along the circumference. The axial injector is at the axial center of the upstream end and the outlet diameter is 5 mm. The solid fuel exists at the position of 25 mm from the upstream end over 150 mm long and its port inner diameter is 40 mm. The throat diameter is 10.5 mm and the exit diameter is 11.9 mm. The geometric swirl number S_g is defined by $A_{port}/(\sum A_{inj})$ for the tangential injectors of the exit area of A_{inj} and the fuel port area of A_{port}.
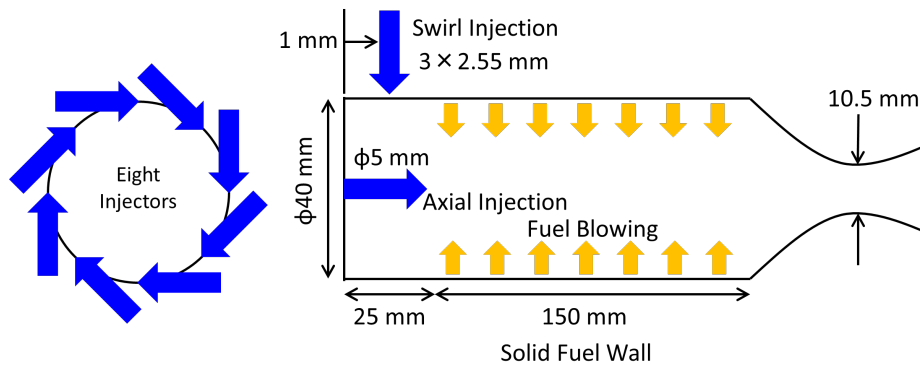
Figure 2: Computational domain

Table 1: Geometrical parameters

Length of combustion chamber	175	mm
Length of fuel	150	mm
Fuel inner port diameter	40	mm
Nozzle throat diameter	10.5	mm
Nozzle exit diameter	11.9	mm
Total area of tangential injector outlets $\sum A_{inj}$	61.2	mm^2
Area of axial injector outlet	19.6	mm^2
Port area A_{port}	1257	mm^2
Geometric Swirl number S_g	20.5	

The 3D structured multi-block grid system illustrated in Fig.3 comprises of 324 thousand cells and is divided into 90 blocks. The number of cell divisions in the circumferential direction is 160, while about 225 and 100 are in the axial and in the radial direction, respectively. The computation of each block is parallelized by means of an message passing interface (MPI). Computation starts from a set of initial conditions (stationary, the temperature of 700K, the pressure of 1.013 MPa) and once sufficient time has elapsed for the flow field to be quasi-steady, an averaged flow field is sampled by taking time-average of instantaneous flow fields. These calculations have been performed on JAXA Supercomputer System generation 2 (JSS2).
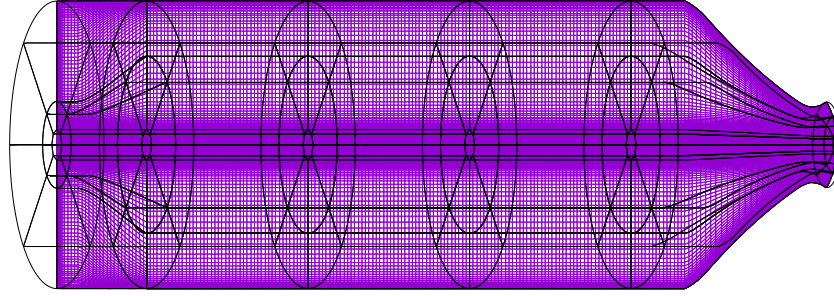
Figure 3: Schematic of 3D structured multi-block grid system

3.2 Boundary conditions

The oxidizer is 100% gaseous oxygen and its total mass flow rate is constant in time and is 15g/s at the temperature of 300K. There are 8 oxidizer inlets each of the size of 3mm × 2.55mm for the tangential injections and 1 oxidizer inlet of the diameter of 5mm for the axial injection. The blowing fuel gas of 100% methane are considered. In fact, the fuel is a solid material such as plastic, rubber or paraffin and so the gasified fuel is a mixture of various hydrocarbons with different molecular weights and the composition of the actual fuel gas mixture is not well understood. In this paper, therefore, methane, which is the simplest hydrocarbon, is used as a fuel to simplify chemical reaction calculation. It can be considered that there is no extreme difference in combustion behavior due to this simplification, since the heat of combustion per unit mass resembles between the general hydrocarbon fuel gas and pure methane. The amount of fuel gas mass flow rate is calculated locally by the following equation utilizing the balance of the heat flux on the fuel surface,

$$\dot{m}_f = \rho_s \dot{r} = \frac{\lambda_g \left. \frac{\partial T}{\partial y} \right|_{y=+0}}{\lambda_s (T_s - T_a)/\alpha_s + \rho_s h_v}, \tag{6}$$

where y is the local moving coordinate normal to the fuel surface, $\dot{m}_f$, the fuel mass flow rate, ρ_s, the fuel density, $\dot{r}$, the fuel regression rate, λ_g, the thermal conduction coefficient of the gas mixture, T_s, the fuel surface temperature, T_a, the temperature of fuel at the (virtual) infinity for the steady-state temperature distribution, α_s, the thermal diffusivity of the fuel, and h_v, the heat of gasification of the fuel. In Eq.(6), the steady-state temperature distribution inside the solid fuel is utilized to evaluate the temperature gradient at $y = -0$. In this study, we set the constant values $\rho_s = 910 \text{kg/m}^3$, $\lambda_g = 0.09 \text{W/m/K}$, $T_s = 600\text{K}$, $T_a = 300\text{K}$, $\alpha_s = 5 \times 10^{-8} \text{m}^2/\text{s}$ and $h_v = 2.5\text{MJ/kg}$. These values are very close to those of polypropylene.

3.3 Simulation cases

For the simulation of the A-SOFT hybrid rocket, three cases have been calculated, where the flow ratio of the oxidizer tangential injections and the axial injection are different. However, unfortunately as for one of these case, the flow field has not yet developed enough to sample the time averaged flow field. Table 2 shows each calculation condition. Here, the mass flow rate of the swirling injection $\dot{m}_{OT}$ represents the total amount from the eight injection ports evenly

Table 2: Calculation conditions

	C1A0	C1A1	C1A2
$\dot{m}_{OT}$ [g/s]	15	7.5	5
$\dot{m}_{OA}$ [g/s]	0	7.5	10
S_e	20.5	5.13	2.28
Temperature [K]	300	300	300

arranged in the circumferential direction, $\dot{m}_{OA}$, the mass flow rate of the axial injection, S_e, the effective swirl number.

The total mass flow rate of these two types of injections is 15g/s in each case. The effective swirl number is defined by

$$S_e = \frac{S_g}{1 + \frac{\dot{m}_{OA}}{\dot{m}_{OT}}^2}.$$

(7)

.

4. Results and discussion

4.1 Bulk properties of time-averaged flow fields

The number of steps until the calculation is completed or the time that has progressed are summarized in Table 3. The criterion of stopping the calculation is basically when the internal pressure settles or becomes the limit cycle, that is when the flow field has developed sufficiently. The time averaging of the flow field starts being taken from the instant for as long as possible. The time-averaged period resulted in each case is summarized in Table 3. Time averaging has been done for **C1A0** and **C1A1**, but not yet been completed for **C1A2**. In Table4, the results of bulk

Table 3: Calculation steps and period

	C1A0	C1A1	C1A2
Number of time steps	5980600	5621100	1563450
Physical duration [ms]	63	82	15
Time-averaged period [ms]	19	40	N/A

properties, such as the combustion chamber pressure, the temperature, the thrust, the oxidizer mass injection flow rate, the fuel mass flow rate, the total incoming mass flow rate, the total outgoing mass flow rate, the specific impulse, the characteristic exhaust velocity, O/F, and the effective swirl number obtained for the two cases are summarized. The

Table 4: Simulation results of time-averaged flow field

		C1A0	C1A1	Unit
Combustion chamber pressure	p_c	0.44	0.38	MPa
Combustion chamber temperature	T_c	1968	1852	K
Thrust	F	43.2	38.1	N
Axial oxidizer injection mass flow rate	$\dot{m}_{OA}$	7.52×10^{-17}	7.50	g/s
Tangential oxidizer injection mass flow rate	$\dot{m}_{OT}$	15.0	7.49	g/s
Total oxidizer injection mass flow rate	$\dot{m}_{OT} + \dot{m}_{OA}$	15.0	15.0	g/s
Fuel blowing mass flow rate	$\dot{m}_f$	10.8	3.01	g/s
Total mass addition rate	$\dot{m}_{OA} + \dot{m}_{OT} + \dot{m}_f$	25.8	18.0	g/s
Mass flow rate at nozzle exit	$\dot{m}_{exit}$	21.8	19.4	g/s
Specific impulse	I_{SP} [a]	171	216	s
Specific impulse	I_{SP} [b]	202	200	s
Characteristic exhaust velocity	C^* [a]	1463	1835	m/s
Characteristic exhaust velocity	C^* [b]	1728	1703	m/s
Oxidizer to fuel ratio	O/F	1.39	4.99	
Effective swirl number	S_e	20.5	5.12	

[a] Evaluated based on total mass addition rate
[b] Evaluated based on nozzle-exit mass flow rate

sum of the oxidizer injection mass flow rate and that of the fuel generation, *i.e.* the total mass addition rate, deviates from the mass flow rate at the nozzle exit by 15% for **C1A0** and by 8% for **C1A1**. Although this deviation is thought to decrease as the flow field sampling is being kept for the time averaging, at this moment we discuss the time-averaged flow field with this error. Since the total mass flow rate influences the evaluation of the specific impulse and the characteristic exhaust velocity, calculations have been performed for two values here. These data are compared with the corresponding chemical equilibrium data obtained by employing NASA CEA web software[15] for the O/F and the combustion pressure obtained from the time-averaged flow field summarized in Table 4, characteristic exhaust speed and vacuum specific impulse at the nozzle exit have been obtained as shown in Table 5. The comparison results about

the efficiencies of I_{SP} and C^* are also summarized in Table 5. According to this, it can be seen that the specific impulse is overestimated in this CFD simulation. A reason to be suspected for this is insufficient sampling time and included error coming from non-steadiness of the averaged flow field.

Table 5: Chemical Equilibrium Analysis

		C1A0	C1A1	Unit
Characteristic exhaust velocity	C^*_{cea}	1615	1684	m/s
Specific impulse	I_{SPcea}	172	168	s
C^* efficiency	$\eta_{C^*}{}^a$	0.906	1.09	
C^* efficiency	$\eta_{C^*}{}^b$	1.07	1.01	
I_{SP} efficiency	$\eta_{I_{SP}}{}^a$	0.997	1.29	
I_{SP} efficiency	$\eta_{I_{SP}}{}^b$	1.18	1.19	

[a] Evaluated based on total mass addition rate
[b] Evaluated based on nozzle-exit mass flow rate

4.2 Axial distribution of cross-sectionally averaged properties of time-averaged flow fields

In Fig.4, the axial distribution of the fuel mass flux generated over the perimeter of the fuel inner port is shown for both **C1A0** and **C1A1** . In both cases, a remarkable fuel mass generation is observed at the tip of the fuel, and it is
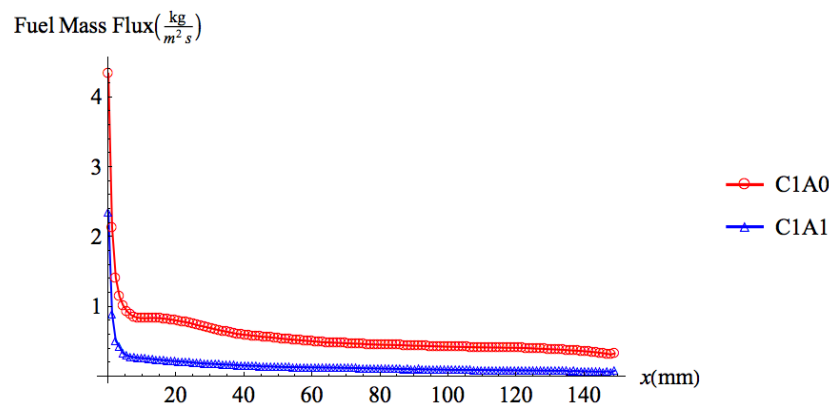
Figure 4: Axial distribution of fuel mass flux averaged over perimeter

a common feature that an abrupt decrease of fuel mass flow is observed along the fuel surface between 5 mm and 10 mm from the tip. This is because the swirling flow promotes the development of the boundary layer. The fuel mass flow rate gently decreases at the downstream. Compared to **C1A1**, about 3.8 times more fuel generation can be seen in **C1A0** corresponding to the fact that the effective swirl number is 5.13 for the former whereas for the latter is it is 20.5. A correlation equation of fuel regression rate was obtained by Ozawa et al. by static firing experiments of A - SOFT hybrid rocket[16] as shown in Eq.(8)

$$\dot{r}[m/s] = 2.557 \times 10^{-5}(1 + Se^2)^{0.0987}G_o^{0.6505}. \tag{8}$$

The fuel mass flow rates calculated by the present simulation are 2.7 times for C1A0 case and 0.987 times for C1A1 case higher than those predicted by these correlations. This result is suggesting the heat transfer evaluation to the fuel is unrealistically large for C1A0 case. Because of this, further investigations are necessary concerning the heat transfer to the fuel surface by the turbulent diffusion in the boundary layer and the resolution of the heat conduction calculation in the viscous sublayer over the fuel surface. Also, it is possible that the results of several seconds of burning obtained in the experiment can differ significantly from those of several tens of milliseconds in the early stages of burning, considering fuel internal heating due to the radiation, variable surface temperature of the fuel, and infinite thickness of the fuel. In the present simulation with assuming the steady-state temperature distribution inside the infinitely-thick fuel may affect the fuel regression rate evaluation through the heat balance on the fuel surface. These are issues to be studied in more detail in the future.

The total pressure averaged over the cross section perpendicular to the center axis varies between the maximum value and the minimum value in the axial distribution and the difference of the maximum and the minimum is only about 0.6% with respect to the bulk average value over the combustion chamber. The bulk value of the combustion chamber pressure is 0.43 MPa for **C1A0** and 0.38 MPa for **C1A1** as shown in Table 4.

On the other hand, as shown in Fig.5, a remarkable change is seen in the cross-sectional average value of the total temperature. This is clearly the effect of combustion and the influence of swirling flow is seen in its distribution. In the case of **C1A0**, the cross-sectional average of the total temperature has a peak in the axial direction with the maximum in the section of about 40 mm from the tip of the fuel, and gradually decreases toward the downstream. The maximum value is about 2400 K. On the other hand, in the case of **C1A1**, the maximum of about 220K is seen at about 100 mm from the tip, but it distributes nearly constant between 50 mm and 130 mm. As a result, the total combustion chamber is 1950 K for **C1A0** and 1840 K for **C1A1** as shown in Table 4.
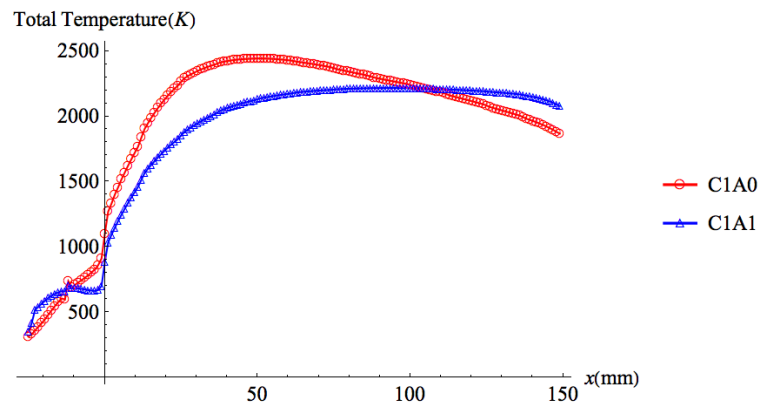
Figure 5: Axial distribution of total temperature averaged over cross-section

4.3 Radial distribution of circumferentially-averaged quantities of the time-averaged flow

Figures 6 and 7 show the radial distribution of the static pressure averaged in the circumferential direction at each axial position x. For **C1A0**, the static pressure is high on the upstream side and in the vicinity of the port wall due to the tangential injection of the oxidizer. This effect disappears about 7 mm in the radial direction from the wall and about 20 mm in the axial direction from the upstream wall . The static pressure gradually decreases as going downstream, but the distribution in the radial direction is almost similar, and a pressure gradient from the center to the wall is seen suggesting strong swirling flow sustains to the downstream.

For **C1A1**, the effect of tangential injection of oxidizer, like **C1A0**, is seen slightly weak. A low pressure part which seems to be influenced by the axial injection of the oxidizer in the vicinity of the central axis can be seen up to about 10 mm from the upstream-end wall. Another feature is to exhibit a uniform static pressure distribution in the radial direction existing downstream of 10 mm in the axial direction, suggesting that the influence of swirling is disappeared there.

COMBUSTION SIMULATION OF A-SOFT HYBRID ROCKET
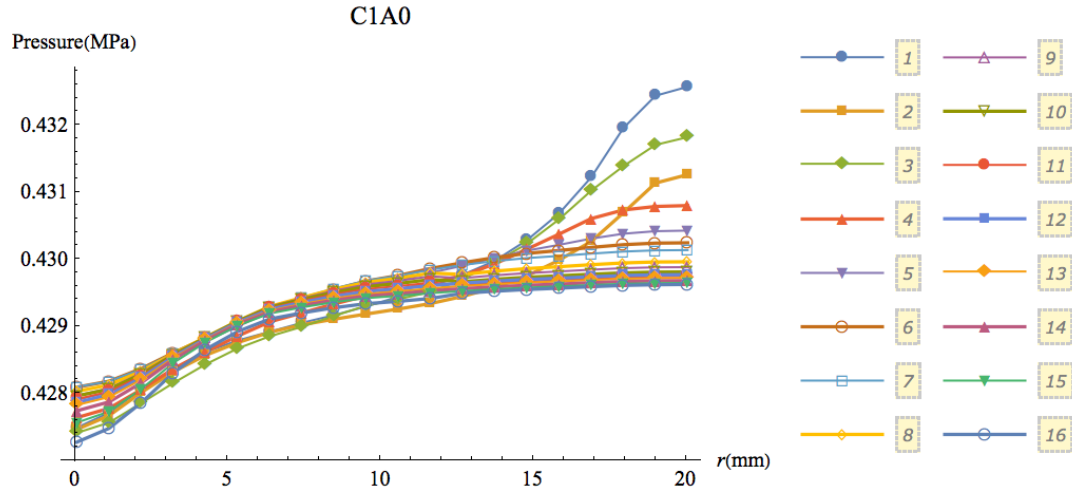
Figure 6: Radial distribution of static pressure (C1A0). $1 : x = -24.999$, $2 : x = -14.074$, $3 : x = -3.15$, $4 : x = 7.775$, $5 : x = 18.7$, $6 : x = 29.624$, $7 : x = 40.549$, $8 : x = 51.474$, $9 : x = 62.398$, $10 : x = 73.323$, $11 : x = 84.248$, $12 : x = 95.172$, $13 : x = 106.097$, $14 : x = 117.022$, $15 : x = 127.946$, $16 : x = 138.871$ [mm]
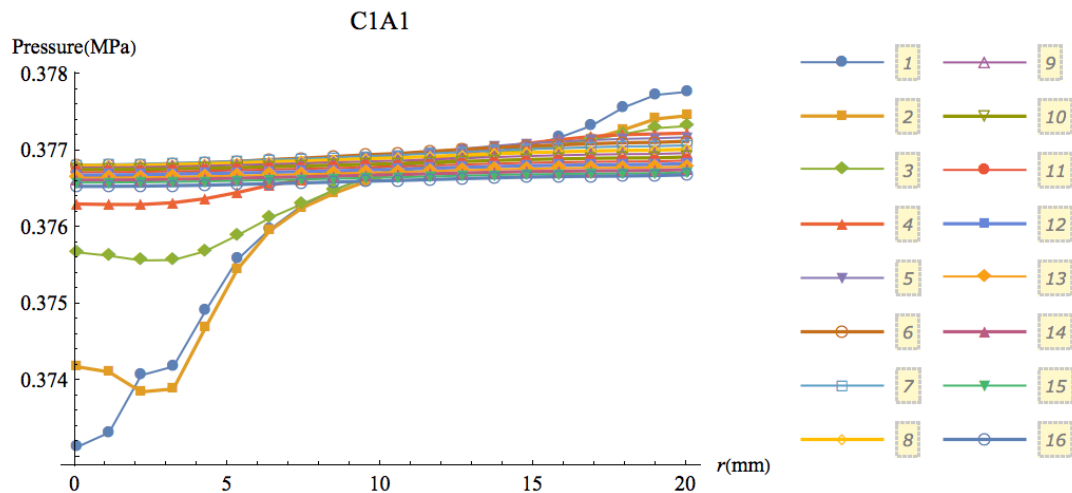
Figure 7: Radial distribution of static pressure (C1A1). $1 : x = -24.999$, $2 : x = -14.074$, $3 : x = -3.15$, $4 : x = 7.775$, $5 : x = 18.7$, $6 : x = 29.624$, $7 : x = 40.549$, $8 : x = 51.474$, $9 : x = 62.398$, $10 : x = 73.323$, $11 : x = 84.248$, $12 : x = 95.172$, $13 : x = 106.097$, $14 : x = 117.022$, $15 : x = 127.946$, $16 : x = 138.871$ [mm]

Figures 8 and 9 show the radial distribution of the axial component of the velocity averaged in the circumferential direction at each axial position. For **C1A0**, two features can be seen. One is that, on the upstream side, the axial component of velocity increases near the side wall with the larger radius and forms one asymptotic velocity distribution as going downstream. The other is that the axial component near the central axis gradually increases and the maximum in the radial distribution appears in the downstream. These indicate that the tangential jet injected along the wall flows downstream and diffuses in the direction of the central axis, as the boundary layer rapidly becomes thick. Then, it is considered that the speed in the axial direction is accelerated around the center axis with the progress of combustion described later.

For **C1A1**, on the other hand, the effect of the jet near the wall is weak, and the jet of the central axis is dominant compared to it. The jet of the central axis decreases the maximum speed as it goes downstream, diffuses in the radial direction, and appears to form a mainstream that is nearly uniform in the downstream of around 60 mm, suggesting less swirling effect in this case. It should be noted that around the central jet, reversal flow exists at x=-13mm to +40mm and disappears as it goes downstream.
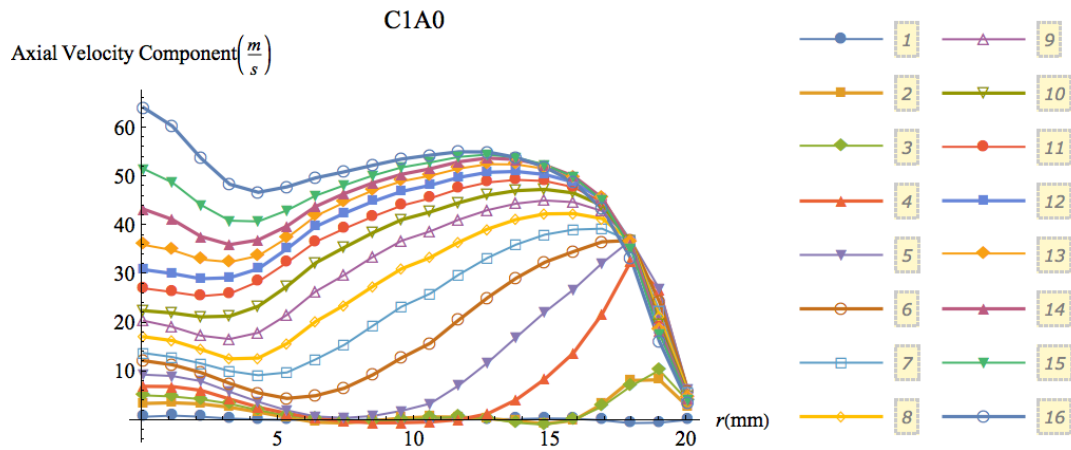
Figure 8: Radial distribution of axial velocity component (C1A0). $1 : x = -24.999$, $2 : x = -14.074$, $3 : x = -3.15$, $4 : x = 7.775$, $5 : x = 18.7$, $6 : x = 29.624$, $7 : x = 40.549$, $8 : x = 51.474$, $9 : x = 62.398$, $10 : x = 73.323$, $11 : x = 84.248$, $12 : x = 95.172$, $13 : x = 106.097$, $14 : x = 117.022$, $15 : x = 127.946$, $16 : x = 138.871$ [mm]
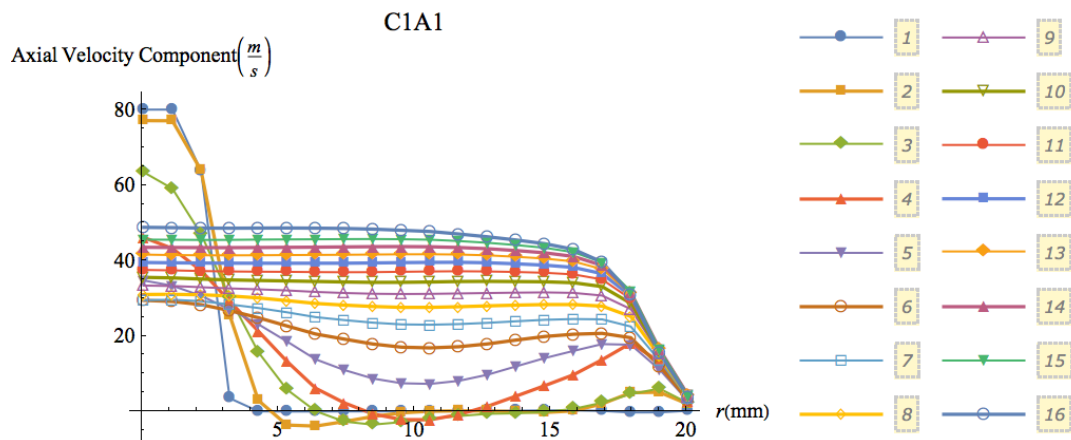
Figure 9: Radial distribution of axial velocity component (C1A1). $1 : x = -24.999$, $2 : x = -14.074$, $3 : x = -3.15$, $4 : x = 7.775$, $5 : x = 18.7$, $6 : x = 29.624$, $7 : x = 40.549$, $8 : x = 51.474$, $9 : x = 62.398$, $10 : x = 73.323$, $11 : x = 84.248$, $12 : x = 95.172$, $13 : x = 106.097$, $14 : x = 117.022$, $15 : x = 127.946$, $16 : x = 138.871$ [mm]

COMBUSTION SIMULATION OF A-SOFT HYBRID ROCKET

Figures 10 and 11 show the radial distribution of the tangential component of the velocity averaged in the circumferential direction at each axial position. For **C1A0**, the oxidizer jet injected in the tangential direction on the upstream side diffuses toward the center axis as going downstream with the radial position of the peak gradually moving towards the central axis, approaching one characteristic profile asymptotically. There seems a rigid vortex velocity profile existing around the central axis within 3 mm in the radius. Regarding **C1A1**, although the effect of the tangential oxidizer jet near the wall is weak, it has similar characteristics as **C1A0**. On the other hand, the tangential component near the central axis is nearly zero due to the central jet, but a strong tangential velocity component appears around the jet. This corresponds to a region in which the axial velocity component flows backward, indicating that there exists a swirl flow toward the upstream. This is a qualitatively different characteristic from **C1A0**. As the central jet diffuses in the radial direction, its circumferential speed decreases and the peak tends to move gradually away from the central axis. This is also the opposite trend to **C1A0**. As it goes to the downstream, a rigid vortex velocity distribution up to the radius of 13 mm remains. It can be seen that the peak of the swirl speed at the most downstream side is about 10 m/s, which is remarkably small as compared with about 60 m/s of **C1A0**.
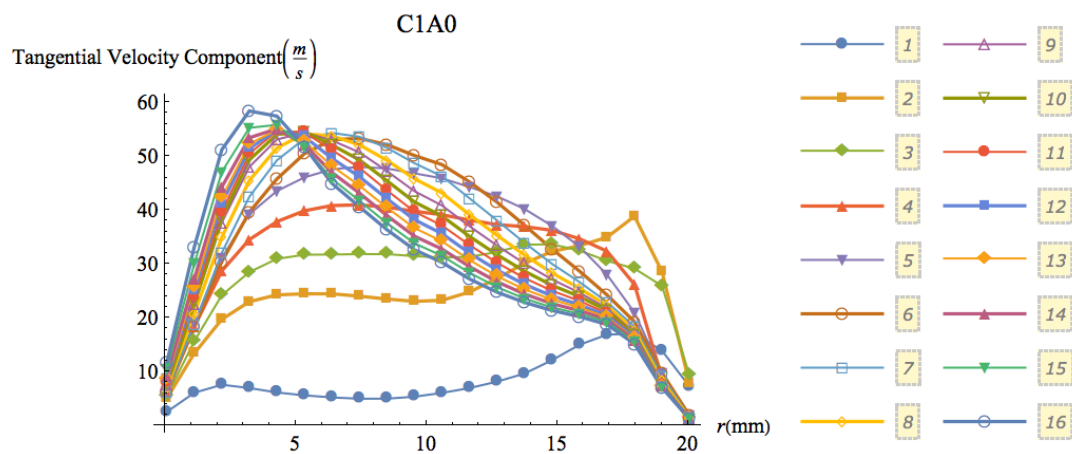
Figure 10: Radial distribution of tangential velocity component (C1A0). $1 : x = -24.999$, $2 : x = -14.074$, $3 : x = -3.15$, $4 : x = 7.775$, $5 : x = 18.7$, $6 : x = 29.624$, $7 : x = 40.549$, $8 : x = 51.474$, $9 : x = 62.398$, $10 : x = 73.323$, $11 : x = 84.248$, $12 : x = 95.172$, $13 : x = 106.097$, $14 : x = 117.022$, $15 : x = 127.946$, $16 : x = 138.871$ [mm]
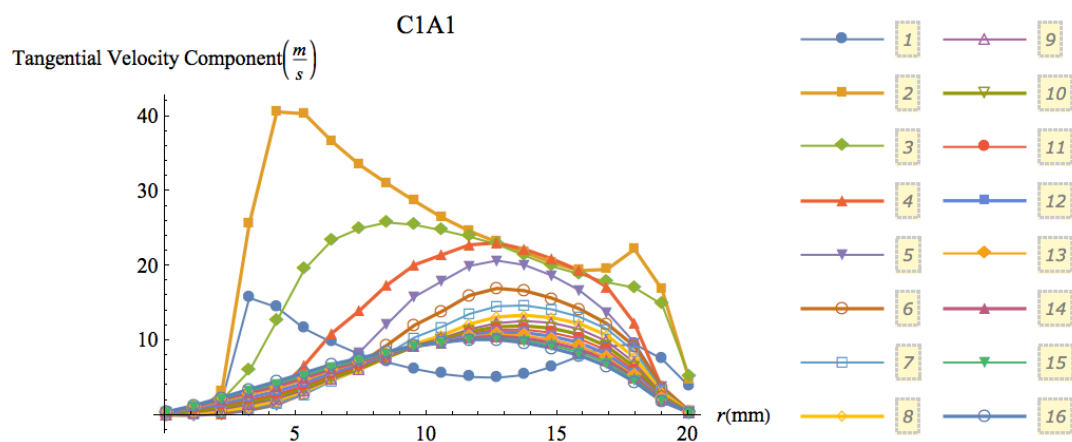
Figure 11: Radial distribution of tangential velocity component (C1A1). $1 : x = -24.999$, $2 : x = -14.074$, $3 : x = -3.15$, $4 : x = 7.775$, $5 : x = 18.7$, $6 : x = 29.624$, $7 : x = 40.549$, $8 : x = 51.474$, $9 : x = 62.398$, $10 : x = 73.323$, $11 : x = 84.248$, $12 : x = 95.172$, $13 : x = 106.097$, $14 : x = 117.022$, $15 : x = 127.946$, $16 : x = 138.871$ [mm]

10

Figures 12 and 13 show the radial distribution of the mixture fraction averaged in the circumferential direction at each axial position. Considering that the mixture fraction at the stoichiometric O/F ratio is 1/3, it can be seen that the mixture fraction increases in the wide region in **C1A0** as it goes to the downstream. This is the influence that the fuel regression rate is increased by the effect of the swirling flow. On the other hand, with regard to **C1A1**, it is suggested that the mixture fraction is low in the whole region and it is not possible to obtain sufficient combustion. It is considered that the main reason is that the fuel retraction rate is too low in this case.
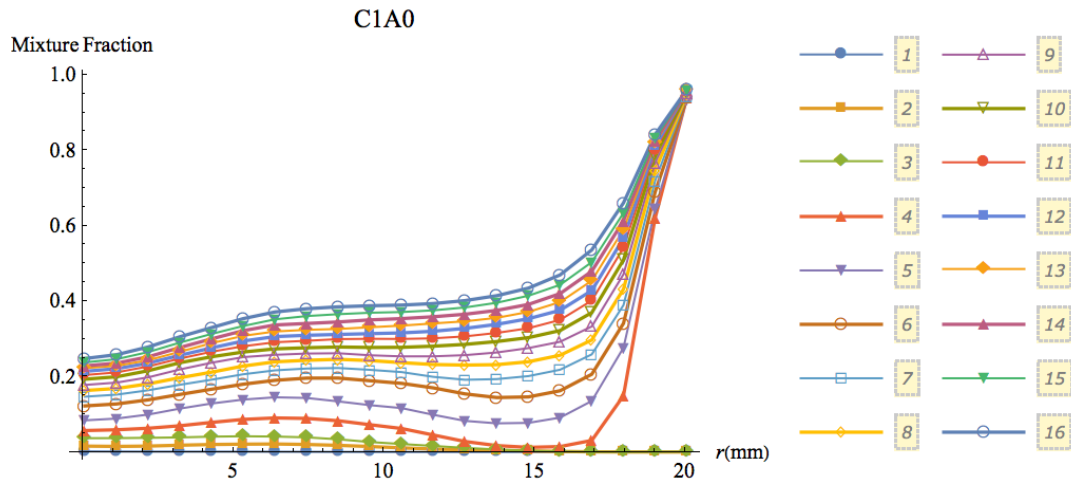
Figure 12: Radial distribution of mixture fraction (C1A0). $1 : x = -24.999$, $2 : x = -14.074$, $3 : x = -3.15$, $4 : x = 7.775$, $5 : x = 18.7$, $6 : x = 29.624$, $7 : x = 40.549$, $8 : x = 51.474$, $9 : x = 62.398$, $10 : x = 73.323$, $11 : x = 84.248$, $12 : x = 95.172$, $13 : x = 106.097$, $14 : x = 117.022$, $15 : x = 127.946$, $16 : x = 138.871$ [mm]
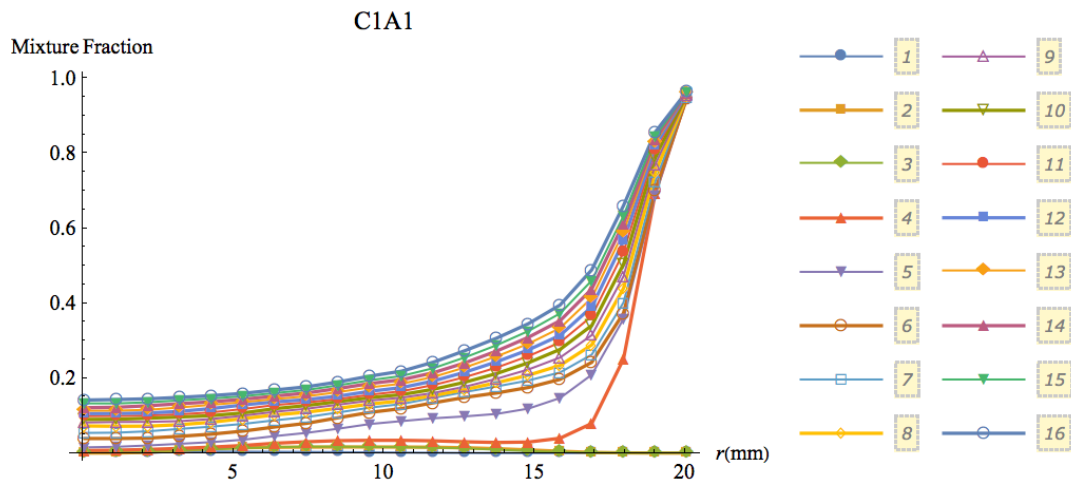
Figure 13: Radial distribution of mixture fraction (C1A1). $1 : x = -24.999$, $2 : x = -14.074$, $3 : x = -3.15$, $4 : x = 7.775$, $5 : x = 18.7$, $6 : x = 29.624$, $7 : x = 40.549$, $8 : x = 51.474$, $9 : x = 62.398$, $10 : x = 73.323$, $11 : x = 84.248$, $12 : x = 95.172$, $13 : x = 106.097$, $14 : x = 117.022$, $15 : x = 127.946$, $16 : x = 138.871$ [mm]

Figures 14 and 15 show the radial distribution of the static temperature averaged in the circumferential direction at each axial position. As expected from the mixture fraction results, it can be seen that the temperature near the central axis rises even at the upstream side for **C1A0** and the temperature at the central axis exceeds 3000 K in the downstream. On the other hand, in the case of **C1A1**, the temperature rise in the vicinity of the central axis does not proceed smoothly, and it is close to 2700K in the downstream.

COMBUSTION SIMULATION OF A-SOFT HYBRID ROCKET
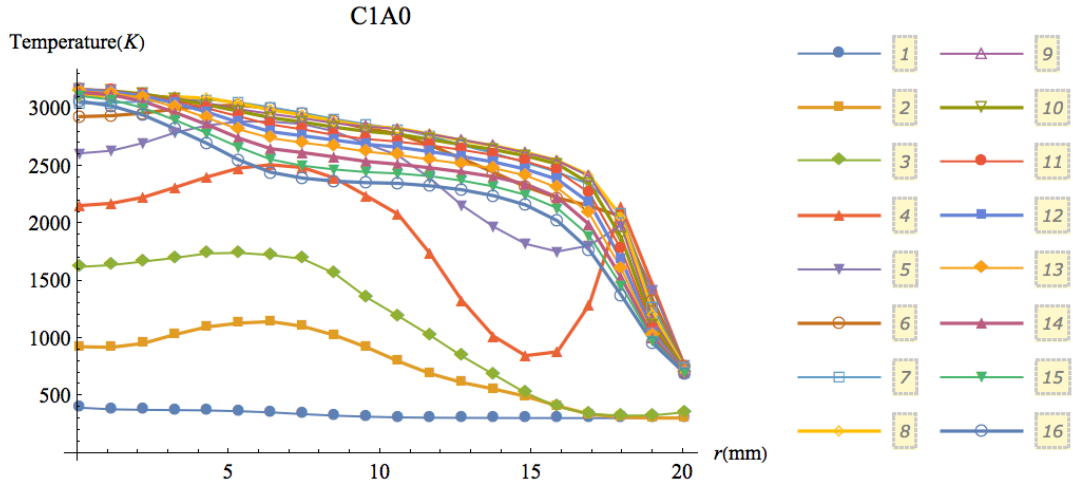
Figure 14: Radial distribution of static temperature (C1A0). $1 : x = -24.999$, $2 : x = -14.074$, $3 : x = -3.15$, $4 : x = 7.775$, $5 : x = 18.7$, $6 : x = 29.624$, $7 : x = 40.549$, $8 : x = 51.474$, $9 : x = 62.398$, $10 : x = 73.323$, $11 : x = 84.248$, $12 : x = 95.172$, $13 : x = 106.097$, $14 : x = 117.022$, $15 : x = 127.946$, $16 : x = 138.871$ [mm]
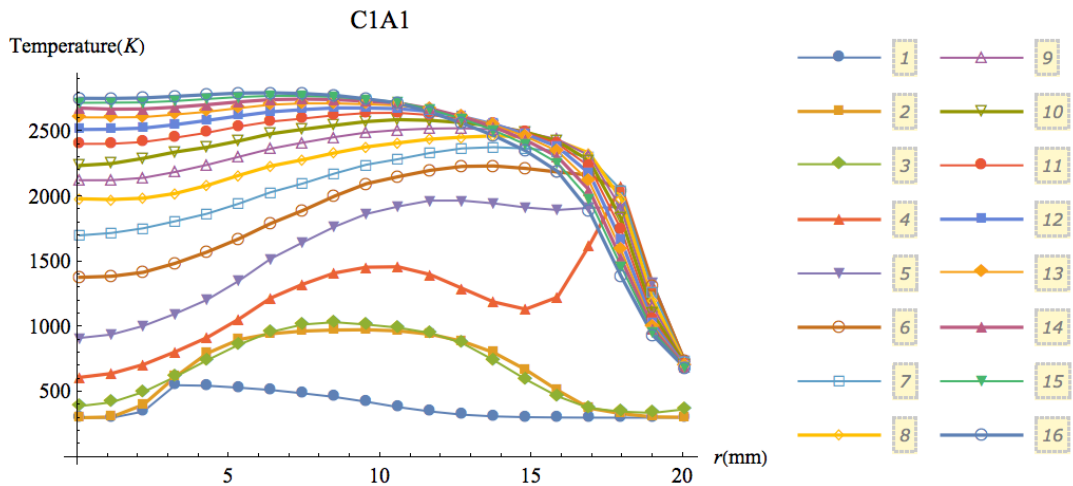
Figure 15: Radial distribution of static temperature (C1A1). $1 : x = -24.999$, $2 : x = -14.074$, $3 : x = -3.15$, $4 : x = 7.775$, $5 : x = 18.7$, $6 : x = 29.624$, $7 : x = 40.549$, $8 : x = 51.474$, $9 : x = 62.398$, $10 : x = 73.323$, $11 : x = 84.248$, $12 : x = 95.172$, $13 : x = 106.097$, $14 : x = 117.022$, $15 : x = 127.946$, $16 : x = 138.871$ [mm]

4.4 Instantaneous flow fields

Figures 16 shows examples of instantaneous flow fields for **C1A0** and **C1A1**. What is shown here is a contour surface where the second invariant of the velocity gradient tensor Q

$$2Q = \frac{\partial u_j}{\partial x_i} \frac{\partial u_i}{\partial x_j} \qquad (i, j = 1, 2, 3) \tag{9}$$

takes a large positive value (here, 10^8 [s^{-2}]). The color represents the magnitude of the velocity component in the axial direction, and the blue region represents the backward flow. Small vortex tubes are visualized in these figures.

12
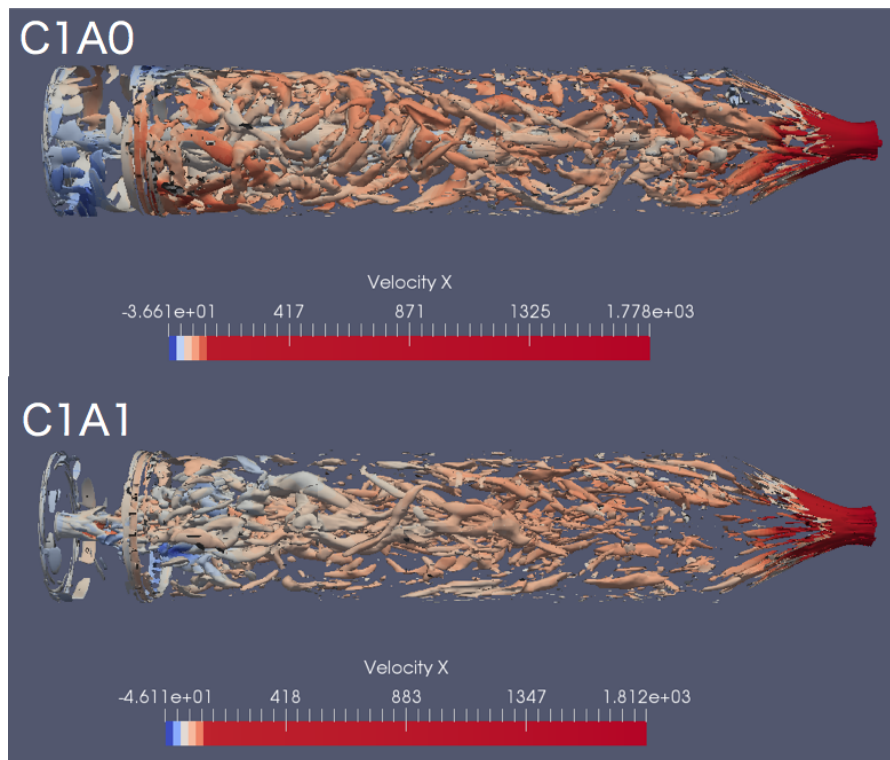
Figure 16: Contour surface of Q of instantaneous flow fields

5. Conclusion and future work

The usefulness of LES for analyzing the hybrid rocket flow field with both swirling and axial oxidizer injections is confirmed. By changing the effective swirl number, the thrust and the O/F change noticeably without changing the total mass flow rate of the oxidizer. The mechanism of this has been found to be due to the change in the qualitative characteristics of the flow field by the overlapping of the tangential injection characteristics and the injection charac- teristics on the central axis. Future tasks such as securing the steady state characteristics of the flow field by taking a sufficient sampling period of the time-averaged solution, refining the analysis of the heat transfer to the fuel including radiation penetration, necessity of unsteady thermal analysis inside the fuel, etc. are thought to be future works.

6. Acknowledgments

References

[1] K.K. Kuo and M. J. Chiaverini. *Fundamentals of Hybrid Rocket Combustion and Propulsion*. American Institute of Aeronautics and Astronautics, Reston, VA, 2007.

[2] F. Barato, M. Grosse, and A. Bettella. Hybrid rocket residuals - an overlooked topic. *AIAA Propulsion and Energy Forum*, AIAA 2014-3753, July 2014.

[3] T. Shimada, K. Kitagawa, M. Kanazaki, S. Yuasa, T. Sakurai, I. Nakagawa, K. Chiba, M. Nakamiya, and K. Ozawa. Study of low-cost 100kg-satellite launcher using hybrid rocket engines. *Space Propulsion*, SP2014-2980899, 2014.

[4] A. Yoshizawa, H. Abe, H. Fujiwara, Y. Mizobuchi, and Y. Matsuo. Turbulent-viscosity modeling applicable to swirling flows, based on a composite time scale with mean flow helicity partially incorporated. *Journal of Turbulence*, 12, 2011.

[5] Mikiro Motoe and Toru Shimada. Numerical simulations of combustive flows in a swirling-oxidizer-flow-type hybrid rocket. *52nd Aerospace Sciences Meeting*, AIAA 2014-0310, 2014.

[6] N. Peters. Laminar diffusion flamelet models in non-premixed turbulent combustion. *Progress in Energy and Combustion Science*, 10(3):319–339, 1984.

[7] H. Pitsch and H. Steiner. Large-eddy simulation of a turbulent piloted methane/air diffusion flame (sandia flame d). *Physics of Fluids*, 12(10):2541–2254, 2000.

[8] H. Pitsch. Flame master, a c++ computer program for 0d combustion and 1d laminar flame calculations, 2004.

[9] Gregory P. Smith, David M. Golden, Michael Frenklach, Nigel W. Moriarty, Boris Eiteneer, Mikhail Goldenberg, C. Thomas Bowman, Ronald K. Hanson, Soonho Song, William C. Gardiner Jr., Vitali V. Lissianski, and Zhiwei Qin. Gri-mech 3.0. `http://www.me.berkeley.edu/gri_mech/`.

[10] E. Shima and K. Kitamura. Parameter-free simple low-dissipation ausm-family scheme for all speeds. *AIAA Journal*, 49:1693–1709, 2011.

[11] R. Borges, M. Carmona, B. Costa, and W.S. Don. An improved weighted essentially non-oscillatory scheme for hyperbolic conservation laws. *Journal of Computational Physics*, 227(6):3191–3211, 2008.

[12] H. Nishida and T. Nonomura. Adi-sgs scheme on ideal magnetohydrodynamics. *Journal of Computational Physics*, 288:3182–3188, 2009.

[13] A. Jameson. Time dependent calculations using multigrid, with applications to unsteady flows past airfoils. *AIAA 91-1596*, 1991.

[14] F. Nicoud and F. Ducros. Subgrid-scale stress modelling based on the square of the velocity gradient tensor. *Flow, Turbulence and Combustion*, 62:183–200, 1999.

[15] NASA. The nasa computer program cea (chemical equilibrium with applications).

[16] K. Ozawa and T. Shimada. Static burning tests on a bread board model of altering-intenisty swirling-oxidizer-flow-type hybrid rocket engine. *AIAA 2016-4964*, 2016.